Diffusion MRS tracks distinct trajectories of neuronal development in the cerebellum and thalamus of rat neonates.

Clémence Ligneul[1]✉, Lily Qiu[1], William Clarke[1], Saad Jbabdi[1], Marco Palombo[2,3]*, Jason Lerch[1,4,5]*

* M.P. and J.L. contributed equally to this work.

Corresponding authors email ✉: clemence.ligneul@ndcn.ox.ac.uk

Affiliations

[1]Wellcome Centre for Integrative Neuroimaging, FMRIB, Nuffield Department of Clinical Neurosciences, University of Oxford; [2]Cardiff University Brain Research Imaging Centre (CUBRIC), School of Psychology, Cardiff University, Cardiff, UK; [3] School of Computer Science and Informatics, Cardiff University, Cardiff, UK; [4]Mouse Imaging Centre, The Hospital for Sick Children, Toronto, Ontario, Canada; [5]Department of Medical Biophysics, University of Toronto, Toronto, Ontario, Canada

Abstract

The brain develops in a nonuniform manner, with local bursts of plasticity. In mammals, the cerebellum remains in a vulnerable developmental state longer than the neocortex, making it a potential hotspot for neurodevelopmental disorders. Cerebellar neurons, and more particularly Purkinje cells, have an altered morphology in forms of autism spectrum disorders or in Down syndrome. However, it is currently impossible to non-invasively assess cerebellar cell-structure during early development. Here we use diffusion-weighted magnetic resonance spectroscopy in combination with microstructural modelling to longitudinally track cerebellar cell-specific development from P5 to P30 in rat neonates. Tracking metabolite diffusion allows us to probe cell-specific developmental trajectories. Additionally, by comparing different analytical and biophysical microstructural models we can follow the differential contribution of cell bodies and neurites during development. The thalamus served as a control region to assess the sensitivity of our method to microstructural differences between the regions. We found significant differences between cerebellar and thalamic metabolites diffusion properties. We report a decreased sphere fraction (or an increased neurite fraction) with age for taurine and total creatine in the cerebellum, marking dendritic growth. Surprisingly, we also report a U-shape trend for segment length (the distance between two embranchments in a dendritic tree) in the cerebellum with age matching morphometry of openly available 3D-Purkinje reconstructions. Results demonstrate that diffusion-weighted MRS probes early cerebellar neuronal development non-invasively.

Introduction

The cerebellum is a well-conserved structure across species and particularly across mammals. The cerebellar cortex is a highly folded structured organized in three layers: the molecular layer (containing the notable Purkinje cell dendritic trees), the Purkinje layer (containing the somas of Purkinje cells), and the granular layer (containing the granule cells). Projections to the deep cerebellar nuclei form the cerebellar white matter. Despite its small size (compared to the cerebrum), it contains more than half of the total brain neurons: this is mainly due to the granule cells, very small and densely packed cells, some of the smallest of the brain, presenting a very simple morphology. On the other hand, the Purkinje cells are one of the largest types of neurons, and most complex cells in the brain. Cerebellar development is protracted[1], and it unfolds progressively from birth (or last trimester of pregnancy) to a few weeks in rodents (or 2 y.o. in humans)[2]. The cerebellum is involved in many basic and high-level functions, from motor control to social skills, and it is known to be affected in a growing number of neurodevelopmental disorders.

During early development, neurons arborise. Their morphology becomes more complex and exhibits denser branching. In rodents, Purkinje cells tree starts growing at birth. In 30 days, they evolve from a simple soma (~10 µm diameter) to a large cell with a highly branched and planar dendritic tree (soma diameter ~20 µm, area ~10,000 μm^2 in the mouse[3]). Purkinje cell morphology can be altered in autism spectrum disorders (ASD), as shown, post-mortem, in humans[4], and in multiple mouse models of ASD. Specifically, with an increased spine density in Tsc1 mutant mice[5], an overgrowth of the dendritic tree and abnormal branching in PTEN KO mice[6], a reduction of the dendritic tree in AUTS2 mice[7]; and generally alterations in developmental disorders[8–11]. While cerebellar cell morphology is informative about brain development, there are very few translational techniques that allow for a non-invasive measure of their morphology.

The thalamus is considered as a relay station in the brain and contains about 60 nuclei on unique pathways. All cerebellar outputs transit by the deep cerebellar nuclei, that projects directly to the thalamus before spreading to the cortex. Some thalamic nuclei are involved in psychiatric disorders, and more specifically, the microstructure of a couple of nuclei are altered in first episode psychosis[12]. Some other nuclei are involved neurodevelopmental disorders (e.g., the lateral reticular nuclei in ASD[13]). Generally, these disorders are associated with an altered thalamic connectivity[12]. Thalamocortical projections are crucial for the cytoarchitectural cortical development[14,15].

Magnetic resonance imaging (MRI) is the gold standard tool to access properties of soft tissues in the body in a safe and non-invasive manner. Diffusion-weighted MRI (dMRI) measures the diffusion properties of water in the brain: constrained and hindered by cell membranes, water diffusion provides an indirect measure of the tissue microstructure[16]. However, water is ubiquitous, and can only partially disentangle the contribution from different compartments. Diffusion-weighted magnetic resonance spectroscopy (dMRS) measures the diffusion properties of metabolites in a large volume of interest. Brain metabolites are mostly intracellular, with some more specific to neurons (e.g., N-acetyl-aspartate, NAA, and glutamate, Glu) and others more specific to glial cells (e.g., choline compounds, tCho, and myo-inositol, Ins), therefore different cellular compartments can be resolved[17]. However, metabolites are 10^4-fold less concentrated than water, which necessitates large measurement volumes for dMRS (typically ~8cm^3 vs ~8mm^3 in dMRI in humans). Morphometric parameters extracted from experiments with multiple diffusion times and multiple diffusion-weightings in dMRS correlate with neuronal and glial morphologies extracted from histological measures in the healthy, adult mouse[18,19]. More specifically, it has been shown that myo-inositol diffusion properties reflect astrocytic morphology in an induced model of astrocytic hypertrophy[20], and in a mouse model of

demyelination where astrocytic activation was expected[21]. Choline compound's diffusion properties were associated with microglial activation in human disease[22], or in an LPS-induced brain inflammation model[23]. However, to the best of our knowledge, very few studies have used dMRS to probe changes in neuronal morphology, and none have attempted to probe neuronal development in early life.

Rodents reach adulthood after a couple of months and are an ideal model to study mammal brain development. Manganese-enhanced MRI (MEMRI) is particularly suited to study whole-brain early development in rodents, providing high structural contrast and speed of acquisition in neonates[1,24], but the method is blind to the nature of the microstructural changes leading to the volumetric changes reported.

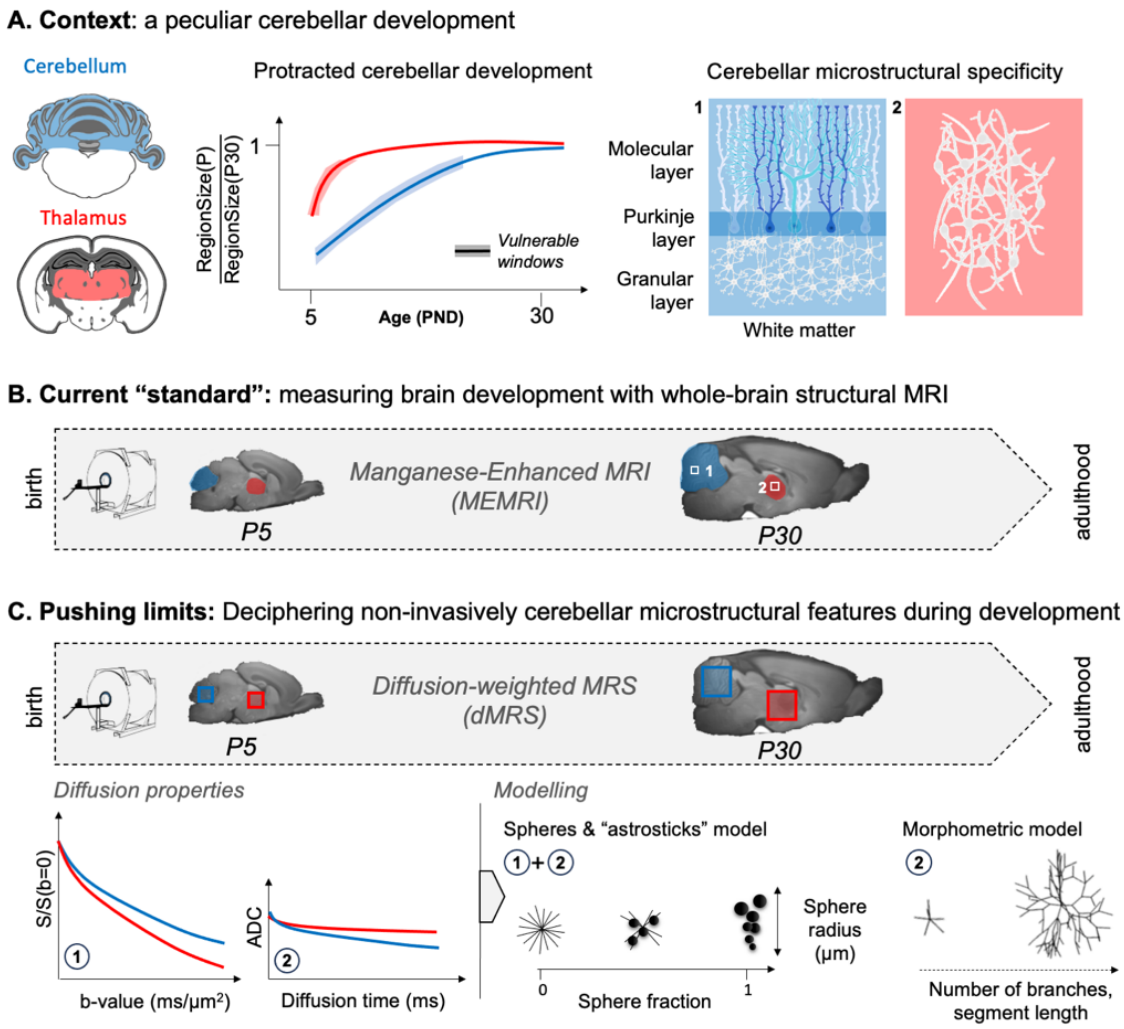

Figure 1: **Overview of the rationale of the study**. (A) Context: the cerebellum exhibits protracted growth compared to other brain regions (e.g., thalamus), making it a particularly vulnerable region for neurodevelopmental disorders. Its specific microstructural organisation (i.e. layered with Purkinje cells and granular cells) changes between birth and adulthood. (B) The current "standard" is to probe regional growth with manganese-enhanced MRI (MEMRI). However, it is not sensitive to the underlying microstructural changes. (C) Pushing limits: diffusion-weighted MRS (dMRS) can potentially assess cell-specific microstructural changes in given regions during development. Different measures of metabolites diffusion properties (apparent diffusion coefficient, ADC, at long diffusion times, signal attenuation, S, at high diffusion weighting, b-values) can be interpreted with biophysical modelling and help characterise the nature of the microstructural changes.

The aim of this study is to propose a non-invasive method to monitor cellular brain development. Neurodevelopmental disorders, or even psychiatric disorders with a neurodevelopmental origin such

as schizophrenia[25], need a better neurobiological characterisation during development[26]. We focus on two regions with different developmental timelines: the cerebellum and the thalamus. As described above, the cerebellum expands greatly after birth, when the Purkinje cells dendritic trees start growing. This slow maturation exposes the cerebellum longer to developmental insults. In contrast to the cerebellum, the thalamus develops relatively quickly, and its neurons expand and complexify more rapidly[1,27].

By contrasting these two regions, we want to assess the sensitivity of the proposed method. We scanned developing rats from postnatal day (P) 5 to P30. We first used MEMRI to confirm the protracted cerebellar development compared to the thalamus. We then acquired diffusion properties of metabolites to probe short- and long-range restriction (i.e., soma restriction and branching). To interpret our data, we applied an analytical and a computational biophysical model to characterise the specific changes in microstructure. We expected monotonic changes in microstructural parameters in both regions, reflecting cell growth, with thalamic properties plateauing earlier than cerebellar properties. This is mostly what we report in our observations. However, we report a U-shape trend for the cerebellar segment length ($L_{segment}$, the distance between two embranchments of a dendritic tree) that match openly available 3D cell reconstructions. We identify total creatine and taurine as more reliable markers for tracking early neuronal development than the usual neuronal markers NAA and Glu because their concentration is too low in neonates. We believe that this is promising method to track early neuronal development, notably in the cerebellum, where microstructure drastically changes postnatally.

Methods

Animals

Experiments were approved by the United Kingdom Home Office. 18 Sprague-Dawley rats (9 females) were scanned at P5, P10, P15, P20 and P30. Pups came from 3 litters (6 pups scanned per litter). Animals were induced with 4% isoflurane in oxygen and anaesthesia was maintained with 1-2% isoflurane in oxygen. Respiration was monitored with a breathing pillow. Temperature was monitored with a rectal probe, which was used as a cutaneous probe from P5 to P20 to avoid any risk of harm. Isoflurane level was adapted to keep the animals at 50-70 rpm and a warm water-circulation heating pad was used to keep the animals at 36-37˚C during scanning. Pups were gently held with foam and protected tape to minimise motion, because the neonatal skull is not suitable for the use of ear bars.

For logistic reasons we could not acquire MEMRI for all litters. Animals from the second litter had manganese-enhanced anatomical scans. To this end, they were intraperitoneally injected with a 50 mg/kg solution of $MnCl_2$ 24 hours prior to the scan. Under the age of P10, the dam received the intraperitoneal injection, and the manganese was transferred to the neonates via the maternal milk.

MRI acquisitions

Data were acquired on a 7T Biospec Bruker MRI scanner (Paravision 360.1, max gradient strength: 660 mT/m), equipped with a mouse quadrature cryoprobe, well-suited for rat neonates. An anatomical scan around the region of interest (thalamus or cerebellum) to place the voxel (T2-weighted, 2D RARE, R=8, 0.2 mm isotropic resolution, TE=33 ms, TR=3500 ms). For 6 animals, this scan was replaced by a whole brain manganese-enhanced anatomical scan (T1-weighted, 3D MGE, TE=2.4 s, TR=62 ms, 0.15 mm isotropic resolution).

Table 1: dMRS acquisition parameters.

dMRS Acquisition parameters					
Mixing time (ms)	**100**		**500**	**750**	**1000**
Diffusion time (ms)	104.25		504.25	754.25	1004.25
b-values (ms/µm^2)	0.035, 3.035, 6, 10, 20, 30		0.17, 3.17	0.26, 3.26	0.35, 3.35
TR (ms)	2000		2500	2750	3000
Total acquisition time	19min		5min	9min	19min
Repetitions	16x(4, 4, 6, 6, 8, 8)		16x(8,8)	16x(10,10)	16x(12,12)
Directions	16				
TE	34 ms (14 ms STE + 20 ms LASER)				
Voxel size					
Age	P5	P10	P15	P20	P30
Volume (µl)	22.05	29.95	48.75	54.60	54.60

dMRS acquisitions

A STELASER (Ligneul et al., MRM 2017) sequence (TE=34 ms, diffusion gradient duration, δ=5 ms) was used for dMRS acquisitions. The voxel was placed in the cerebellum for 9 pups, and in the thalamus

for the other 9 pups. Voxel size was increased with age to follow brain growth. Diffusion-weighted spectra were acquired at 4 mixing times (TM) and 2 b-values (c.f. Table 1 for detailed parameters): a small "b_0" used as a crusher for the stimulated echo, and b_0+3 ms/µm^2. Higher b-values were also acquired at the shortest diffusion time to probe restriction within cell bodies and enable inference of cell fraction and radius.

Processing

dMRS

Processing was achieved with a custom Matlab (The Mathworks) routine:

- Signal from different coils were combined, the phase between elements was determined from the water signal at the lowest b-value and shortest diffusion time.
- Outliers were identified and discarded, as described in[28].
    - For each transient i, the mean absolute upfield signal (range 1.9-4.5 ppm), $M_{up}(i)$ was computed.
    - Transients affected by motion are characterised by a clear drop of $M_{up}(i)$. Transients falling below the median(M_{up}) - 3xMAD threshold were discarded.
    - Experiments at high b-values are more susceptible to changing gradient direction (particularly if the voxel contains white matter tracts). To predict its effect across b-values and overcome the small number of acquisitions per unique condition (i.e. a (b-value, direction) pair), a diffusion kurtosis tensor was computed based on M_{up}. The MAD calculated at b=0 was used as a "ground truth" MAD and was reported to higher b-values (per direction). High b-values acquisitions are more easily corrupted by motion and therefore present an artificially high MAD.
- Individual transients were corrected for phase and frequency drifts and powder-averaged via an arithmetic mean. In general, metabolites signal was visually detectable on single transients (with a line-broadening of 5 Hz), except at b=20,30 ms/µm^2 at P5, rendering these acquisitions more susceptible to motion artefacts.
- Any water residual was removed using a singular value decomposition method centred around the water region. If the baseline was heavily distorted despite this step due to very poor water suppression, the acquisition was discarded from the analysis.

Spectra were subsequently fitted with LCModel. The simulated basis set contained the following metabolites: Ace, Ala, Asp, Cr, GABA, Gln, Glu, Gly, GPC, GSH, Ins, sIns, Lac, NAA, NAAG, PCho, PCr, Tau, PE, and included a macromolecules (MM) baseline acquired experimentally (double-inversion recovery and b=10 ms/µm^2).

Diffusion properties of NAA+NAAG (tNAA), Glu, Cr+PCr (tCr), Tau, GPC+PCho (tCho) and Ins are reported. In order to model both signal compartmentalisation and restricted diffusion by cell membranes, we investigated metabolites diffusion through two sets of measurements: i) the direction-averaged signal decay as a function of the diffusion weighting b, keeping the diffusion time constant at 104.25 ms (time between diffusion gradients Δ fixed at 105.91 ms and δ fixed at 5 ms) and varying the strength of the diffusion-sensitizing gradients; and ii) the apparent diffusion coefficient (ADC) as a function of increasing diffusion time (keeping δ fixed at 5 ms). For the measurements i), data are reported as the ratio S(b)/S(b=0). For the measurements ii), ADCs diffusion time dependencies are reported. ADCs are calculated following $ADC = \frac{-1}{b-b_0}\log\frac{S(b)}{S(b_0)}$. Negative ADCs were systematically removed as they point to a quantification error.

MEMRI

The three first echoes of each MGE acquisition were averaged and denoised using the DenoiseImage function from the MINC toolbox, based on[29]. For each time point, the best-looking image was taken as the initial model and transformed into the Fischer atlas[30] space. Images were then processed using registration_tamarack.py with the MAGeT segmentation in the available Pydpider pipelines[31]. Due to the large deformations between P30 and P5, the P30 timepoint could not be used as a reference. An adequate atlas from P15 was generated in a couple of iterations (using a P20 atlas as intermediary). It was then used as a reference atlas and reference timepoint for the pipeline. The olfactory bulb and the more frontal parts were poorly registered because the image often had an intensity drop there, but it did not affect the registration of caudal regions, such as the cerebellum and the thalamus. Image with strong intensity differences, or corrupted by motion were removed from the analysis. The registration did not work well at P5, even when attempting to use an atlas generated at P10 (that is already slightly distorted).

Analysis

Signal decays at high-b values (at TM=100 ms) and ADCs at varying diffusion times were fitted together with a spheres and "astrosticks" (corresponding to randomly oriented sticks) model using the functions implemented in DIVE (https://git.fmrib.ox.ac.uk/fsl/DIVE). We fitted the signal to:

$$\frac{S}{S_0} = f_{sphere} * S_{sphere}\left(D_{intra}, R_{sphere} | b_{value}, t_d, \delta\right) + (1 - f_{sphere}) * S_{sticks}(D_{intra} | b_{value})$$

Free parameters were R (sphere radius) and f_{sphere} (sphere fraction). D_{intra} (i.e. the metabolite intracellular free diffusivity) was fixed for both compartments at 0.5 $\mu m^2/ms$. Previous studies measuring brain metabolites diffusion properties at ultra-short diffusion-times[32,33] estimated the intracellular free diffusivity at 0.5-0.6 $\mu m^2/ms$ for most metabolites (except Tau). However other studies using different (less direct) approaches reported lower D_{intra}[18,19], hence we tested a range of reasonable D_{intra}. D_{intra} was fixed 0.3, 0.4, 0.5, 0.6, 0.7 and 0.8 $\mu m^2/ms$. RMSEs between model fit and data were equivalent for all D_{intra}, except for Taurine in the thalamus where increasing D_{intra} improved the fit, particularly until D_{intra}=0.5$\mu m^2/ms$. Moreover, parameters estimation was unrealistic for low D_{intra}. Increasing D_{intra} between 0.5 $\mu m^2/ms$ and 0.7 $\mu m^2/ms$ did not change the trend of the results, except for taurine in the thalamus (see **Figure S0** and Discussion). The fit was made robust to missing data (when excluded during processing).

To test for the model accounting best for our data, we tested different analytical models. RMSE between model fit and data were calculated for "astrosticks" only (1 free parameter, D_{intra}), "astrocylinders" (corresponding to randomly oriented infinite cylinders, 2 free parameters: D_{intra} and cylinder radius), spheres and astrosticks without constraint (3 free parameters) and spheres and astrosticks with D_{intra} fixed at 0.5 $\mu m^2/ms$ (**Figure S0**). RMSE were the lowest for spheres and astrosticks, and were very similar with and without the D_{intra} constraint. Hence the model with the least free parameters was chosen. Moreover, the results from the constrained spheres and astrosticks model were more stable and physically meaningful with the constraint on D_{intra}.

Long diffusion times:

Average ADCs at varying diffusion times were fitted with the morphometric model introduced in (Palombo et al., PNAS, 2016). Modeling was performed using the dictionary generated for (Ligneul et al., NeuroImage, 2019) with TM = 100, 750 ms predicted by interpolation, and a random forest regressor ('treeBagger' function in MatlabR2020b, with tree depth = 20; number of trees = 200 and other model hyper-parameters as per default) trained in a fully supervised fashion, using the ADCs

time dependencies as input and the ground truth morphological parameters as targets; as loss function the mean squared error between predicted and ground truth parameters values was used. Parameters fitted were D_{intra}, N_{branch}, $L_{segment}$, SDN_{branch} and $SDL_{segment}$. Boundaries for fitting the model to data were respectively [0.1, 1], [2, 25], [5, 100], [2, 3] and [5, 10]. Given the data noise, only $L_{segment}$ and D_{intra} are estimated robustly. Fits for all parameters are shown in supplementary.

Statistical analyses

Statistical analyses were run with R, using the "lmerTest[34] package. To assess whether diffusion properties were significantly different in the 2 regions during development, we applied a linear mixed effect model to the parameters extracted from the spheres + "astrosticks" model (sphere fraction and sphere radius), using age and region as fixed effects, and a random intercept for pups ID. An analysis of variance enabled to identify whether the inclusion of an interaction term age*region was necessary or not. Results were corrected for multiple hypotheses testing with a Bonferroni correction (6 metabolites,2 parameters = 12 hypotheses). The threshold corrected p-value is $4.2e^{-3}$ for α=0.05 and $8.3e^{-4}$ for α=0.01.

Results

Structural imaging confirms protracted cerebellar growth.

Representative slices from intra-age non-linear registration are shown in **Figure 2A**, underlying the cerebellar unfolding. Both cerebellar and thalamic volumes are just below 50µl at P5 (**Figure 2B**). However, the segmentation at P5 is poor, as explained in Methods (**Figure S1**), hence data at this time point should be treated cautiously, although the cerebellum and the thalamus, that are medial line structures, are less affected by the atlas distortions.

The cerebellum triples in volume, between P5 and P30, reaching 90% of its P30 volume at P20, while the thalamus reaches 90% of the P30 volume at P15.

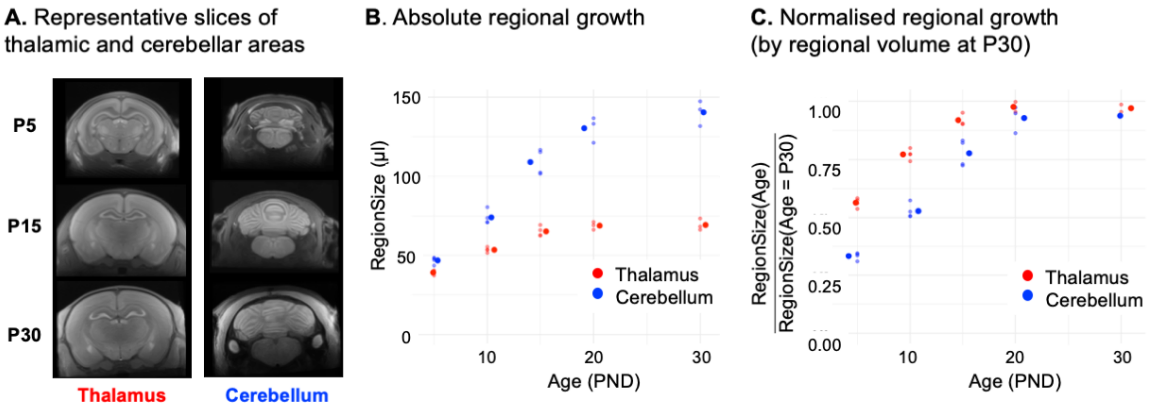

Figure 2: **Manganese-enhanced MRI confirms protracted cerebellar growth in rat pups.** (A) Representative slices around the thalamus and cerebellum of non-linearly averaged images acquired at P5, P15 and P30. (B) Absolute volumetric changes shown for the segmented thalamus and cerebellum. (C) Normalised volumetric changes. Volume at each age is normalised by the P30 volume.

Metabolic profile changes with age.

The metabolic profile changes noticeably between P5 and P30 as shown in **Figure 3A**. The absolute metabolites' concentrations estimated by LCModel on the b_0 averaged spectra shown in **Figure 3A** were normalised by the absolute macromolecules' concentration, MM (**Figure 3C**). Between P5 and P30, metabolites/MM ratios increase for tNAA, Glu, Gln and Ins, and decrease for Tau, Gly, PE and tCho. These results generally match the metabolic concentrations measured with gold-standard classical MRS in the striatum, cortex and hippocampus of developing rats reported in[35]. We observe that tCr/MM increases strongly in the cerebellum between P5 and P30 but appears stable in the thalamus, while (Tkac et al., MRM, 2003) reported a 30% increase between P7 and P28 in the 3 ROIs. However, they also reported a 30% increase of the macromolecular content during this developmental period, matching our tCr/MM observation in the thalamus.

Macromolecular signal attenuation underlines a possible motion artefact at P5 in the cerebellum.

In the cerebellum, metabolites' signal attenuation at P5 is always much stronger and quite far off the other time points. The macromolecules' signal attenuation at high b-values is supposed to remain low[36] and can be used as an internal probe for motion artefact[32]. However, the macromolecules' signal attenuation is quite strong at P5 in the cerebellum (**Figure 3B**), pointing out to a residual motion artefact despite careful processing. The spectroscopic signal in individual transients was too low at high b-values, notably in the cerebellum: it is possible that the spectral realignment failed.

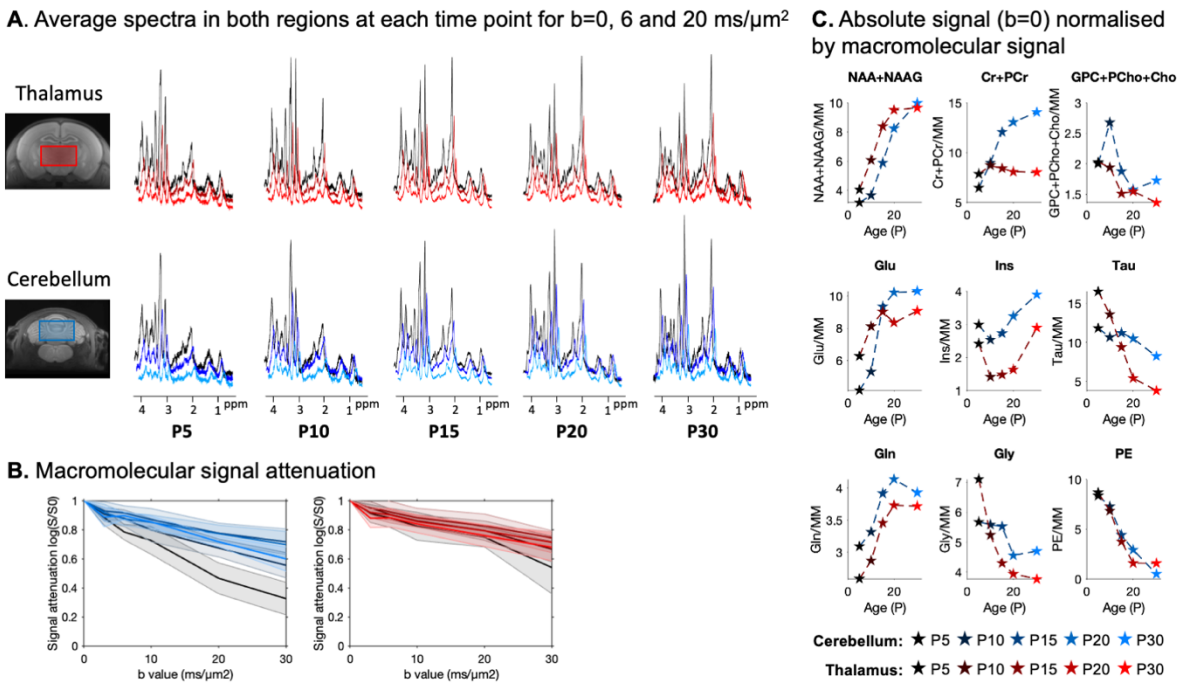

Figure 3: **Metabolic profile changes postnatally**. (A) Spectra were binned per time point, region and b-value and averaged after phase and frequency correction. The SNR is clearly lower at P5/P10 in both regions: the voxel is about half of the P30 voxel size, and more animals were outliers. The SNR is also lower at P30: the rat size was slightly too big for the mouse cryoprobe at this age, so the skull is not at the top of the probe and the sensitivity is suboptimal. (B) Mean macromolecular signal attenuation at high b-values for each time point coming from the LCModel fit. The shaded error-bars represent the standard deviation from the mean. Signal attenuation in the cerebellum at P5 is stronger: it likely corresponds to residual motion artefact. (C) Spectra at b=0 ms/µm² displayed in (A) were quantified with LCModel and absolute metabolite concentrations were normalised by the absolute macromolecular concentration and levelled to get Signal(tCr,P30)/Signal(MM,P30)=8.

Metabolites diffusion properties differ between regions and change with age.

Signal attenuations up to b=30 ms/µm² and ADCs at TM=100-1000 ms measured in the thalamus (**Figure 4A**) and in the cerebellum (**Figure 4B**) are shown for tNAA, Glu, tCr, Tau, tCho and Ins. These diffusion properties differ between both regions at each age (see **Figure S2** for a region-to-region visual comparison). For most metabolites (except tCho), the signal attenuation is stronger in the thalamus, suggesting a less restricted diffusion in the thalamus compared to the cerebellum. There is also a trend for lower signal attenuation and lower ADCs with increasing age, suggesting increasing restriction effects. This is particularly striking for taurine in the thalamus. To give an estimation of the MRS fit performance, CRLBs are given for tNAA, Glu, tCr, Tau, tCho and Ins for the different diffusion conditions in **Table S1**.

Biophysical modelling underlines different developmental trajectories between cerebellum and thalamus.

Data were fitted with a spheres + "astrosticks" model and a morphometric model. The spheres + "astrosticks" model captures diffusion within spheres (representing cell bodies) and randomly oriented sticks (representing cell processes/neurites): parameters extracted are sphere fraction (or equivalently neurite fraction) and cell radius. The parameters space (sphere radius vs sphere fraction) is represented in the 3rd column of **Figure 4A** (cerebellum) and **Figure 4B** (thalamus) for tNAA, Glu, tCr, Tau, tCho and Ins at all ages (see **Figure S3** for a region-to-region visual comparison).

Mean values and standard deviations are reported in **Table 2**, along with the results from the linear mixed effect model ~ Age, Region + (1|PupID). The fits on averaged data, for binned spectra by age and region, are shown in **Figure S4**.

The morphometric model, only applied to averaged ADCs at long t_d, interprets diffusion in branched structures: the segment length, $L_{segment}$ is reported on the last column of **Figure 4A/B** (see **Figure S5** for a region-to-region visual comparison and **Figure S6** for all parameters: D_{intra}, N_{Branch}, $L_{segment}$).

<u>Neuronal markers</u>: tNAA and Glu are primarily concentrated in neurons in adulthood.

- Thalamus: The sphere fraction and radii estimated from tNAA and Glu diffusion properties do not change much with age. For both metabolites, f_{sphere} is around 0.25 and R decreases to ~ 5-6µm. $L_{segment}$ is stable with age for tNAA, but presents a dip at P15-P20 for Glu.
- Cerebellum: The sphere fraction and radii estimated from tNAA diffusion properties vary with age. f_{sphere} nears 0.5 in the cerebellum and R decreases below 5µm for tNAA and Glu. $L_{segment}$ tends to decrease up to P15 for both tNAA and Glu in the cerebellum.

Between regions, sphere fraction differs significantly (**Table 2**).

<u>Glial markers</u>: tCho and Ins are primarily concentrated in glial cells in adulthood. The general trend is a high sphere fraction (~0.7-0.9) for Ins and moderately high (~0.5-0.6) for tCho. Radius estimated from tCho differs significantly between regions. Note the trend of decreasing sphere fraction in the cerebellum with age.

<u>tCr and Tau</u>: these metabolites are not known to be compartmentalised in a specific cell-type. *

- Thalamus: Parameters estimates for tCr diffusion properties do not change substantially with age (f_{sphere}~0.35, R~6.5µm). Taurine parameters estimation varies a lot with age (radius drastic decrease and increased sphere fraction).
- Cerebellum: f_{sphere} decreases from 0.63 (P10) to 0.41 (P30), but R is stable. Taurine follows a similar pattern, although with overall lower sphere fractions (0.43 at P10 to 0.29 at P30). $L_{segment}$ increases in the cerebellum from P10 for tCr but increase only from P15 for Tau.

Between regions, the sphere fraction differs significantly for both metabolites, but only taurine exhibits a significant change with age, and this change is different between regions (significant interaction term). For taurine only, radius is significantly different between regions and changes significantly with age.

.

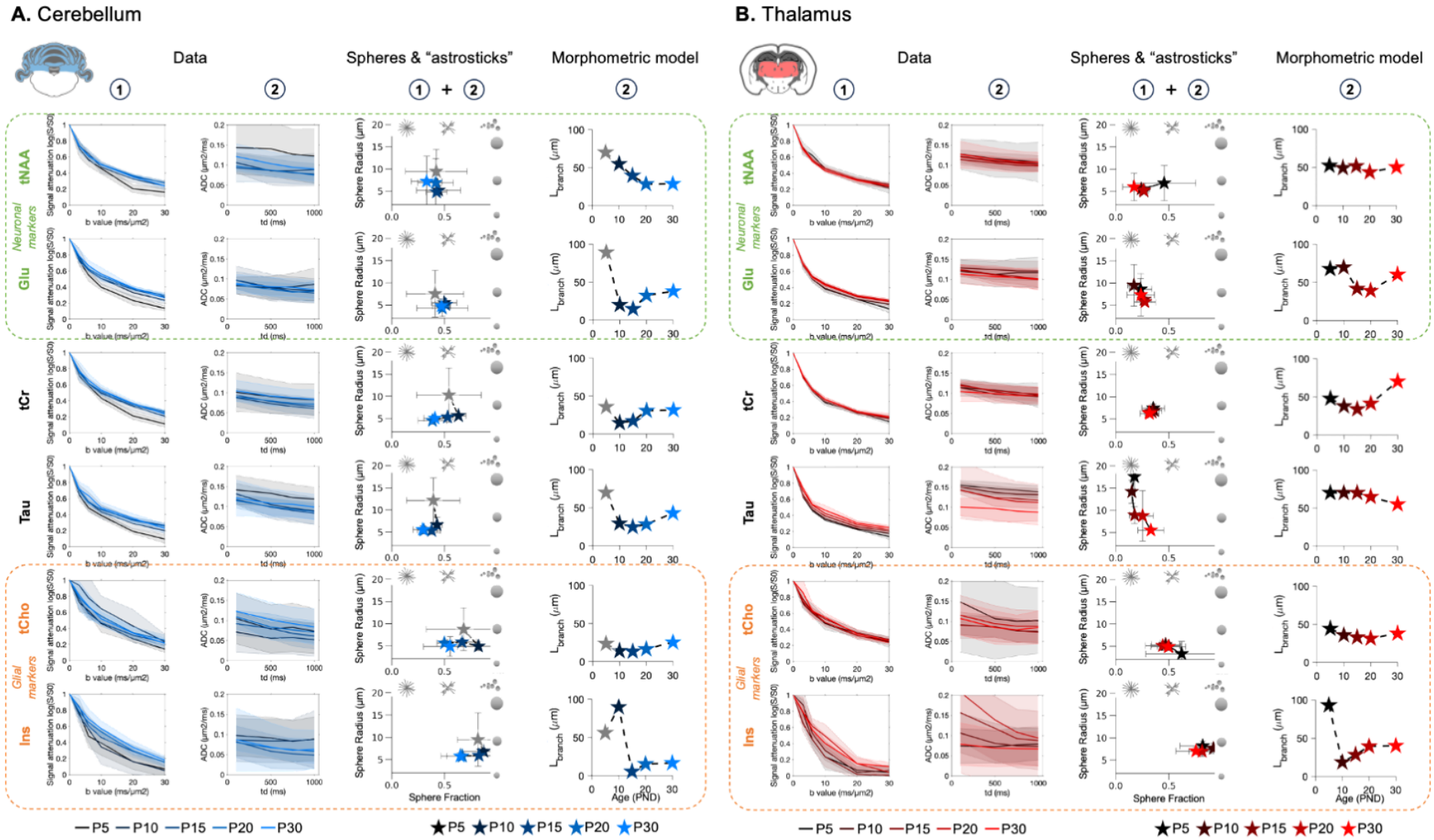

Figure 4: Biophysical modelling issued from metabolites diffusion properties shows differential developmental trajectories in the cerebellum (A) and in the thalamus (B). The first column (A,B) reports the signal attenuation as a function of b-value at TM=100ms, and the second column reports the ADC varying with diffusion time. Shadowed error bars represent the standard deviations. Modeling results from the spheres+"astrosticks" model is reported in the third column (A,B). P5 is shaded in the cerebellum due to possible motion artefact. The parameter space (sphere fraction, sphere radius) is displayed. Error bars represent the standard deviations. L_{length}, modeling output from the morphometric model is shown in the fourth column (A,B). P5 is shaded in the cerebellum due to possible motion artefact.

Table 2: Mean values and standard deviations for parameters extracted from the spheres + "astrosticks" model (sphere radius and sphere fraction). Statistics come from a linear model accounting for age and region as fixed effect. The interaction term was included only if it improved the fit significantly (c.f. Methods). p-values highlighted in yellow pass the α=0.05 threshold after multiple comparison correction and green p-values pass the α=0.01 threshold.

	CEREBELLUM					**THALAMUS**					lmer ~ Region, Age + (1|PupID) *p-values*		
Age (PND)	5	10	15	20	30	5	10	15	20	30	Region	Age	Region:Age
	NAA+NAAG					NAA+NAAG							
Radius (µm)	9.44	5.18	4.78	6.92	7.21	6.84	5.52	5.05	5.24	5.97	2.60E-01	5.08E-01	
std(Radius) (µm)	4.91	1.10	0.58	5.34	5.66	3.96	0.77	0.59	0.55	3.08			
Fraction	0.42	0.45	0.42	0.42	0.33	0.46	0.24	0.27	0.26	0.17	6.50E-04	4.66E-03	
std(Fraction)	0.29	0.21	0.10	0.17	0.15	0.30	0.08	0.04	0.03	0.11			
	Glu					Glu							
Radius (µm)	7.50	5.49	5.04	4.26	4.79	8.57	9.46	6.26	5.71	7.32	7.16E-03	1.61E-02	
std(Radius) (µm)	5.29	0.91	0.24	1.88	0.12	2.42	4.70	0.62	0.62	4.82			
Fraction	0.41	0.50	0.51	0.48	0.47	0.23	0.17	0.27	0.28	0.24	7.02E-06	3.81E-01	
std(Fraction)	0.27	0.12	0.04	0.24	0.09	0.11	0.06	0.07	0.10	0.13			
	Cr+PCr					Cr+PCr							
Radius (µm)	10.28	5.61	5.31	4.54	5.07	7.38	6.87	6.53	6.45	6.18	1.14E-01	2.52E-01	1.65E-02
std(Radius) (µm)	6.08	0.58	0.32	0.78	0.50	0.92	0.57	0.31	0.69	0.67			
Fraction	0.54	0.63	0.53	0.39	0.41	0.35	0.36	0.34	0.31	0.32	2.16E-05	3.88E-01	5.07E-02
std(Fraction)	0.31	0.07	0.05	0.14	0.10	0.11	0.07	0.02	0.04	0.09			
	Tau					Tau							
Radius (µm)	12.14	6.63	5.32	5.41	5.56	17.57	14.18	8.90	8.73	5.50	4.56E-06	4.47E-11	9.65E-03
std(Radius) (µm)	5.13	1.76	0.83	0.83	0.85	2.97	2.58	1.88	5.67	0.57			
Fraction	0.39	0.43	0.38	0.31	0.29	0.18	0.15	0.18	0.25	0.33	1.75E-09	3.69E-04	3.10E-05
std(Fraction)	0.25	0.05	0.08	0.06	0.09	0.03	0.03	0.05	0.10	0.12			
	tCho					tCho							
Radius (µm)	8.68	4.88	5.83	5.59	4.83	3.28	5.35	4.91	5.10	4.86	2.93E-04	2.96E-01	5.06E-03
std(Radius) (µm)	4.83	1.03	0.53	0.58	2.24	2.77	0.59	0.56	1.07	0.87			
Fraction	0.68	0.82	0.67	0.50	0.55	0.62	0.47	0.50	0.44	0.50	2.93E-03	2.71E-02	
std(Fraction)	0.35	0.20	0.14	0.07	0.25	0.34	0.13	0.11	0.16	0.16			
	Ins					Ins							
Radius (µm)	9.47	6.81	5.89	5.74	5.75	8.18	7.60		6.93	7.00	9.89E-02	1.41E-02	
std(Radius) (µm)	6.03	0.56	0.51	0.60	0.75	1.05	1.16		1.14	0.79			
Fraction	0.82	0.87	0.83	0.67	0.65	0.82	0.92		0.81	0.76	2.24E-01	1.75E-02	
std(Fraction)	0.19	0.22	0.15	0.15	0.18	0.21	0.14		0.13	0.19			

Discussion

As in[1] we used MEMRI to validate the protracted development of the cerebellum in rat neonates[2], unfolding and tripling volume between P5 and P30. Cell-specific cerebellar and thalamic microstructural features during early development in rat neonates were assessed with dMRS. We specifically report diffusion properties for neuronal markers tNAA and Glu, glial markers tCho and Ins, and tCr and Tau, which are not known to be more concentrated in one compartment. Metabolites exhibit significantly different diffusion properties between regions, demonstrating the relevance of dMRS to probe early cell structure development. The sphere fraction is notably higher in the cerebellum for metabolites compartmentalised fully (tNAA, Glu) or partially (tCr, Tau) in neurons, suggesting the cell-body dense granular layer of the cerebellum. The sphere fraction possibly reflects the relative volume of sphere-like structure (e.g., cell bodies) compared to the relative volume of fibrous structures (e.g., cell processes), illustrated in **Figure 5A**.

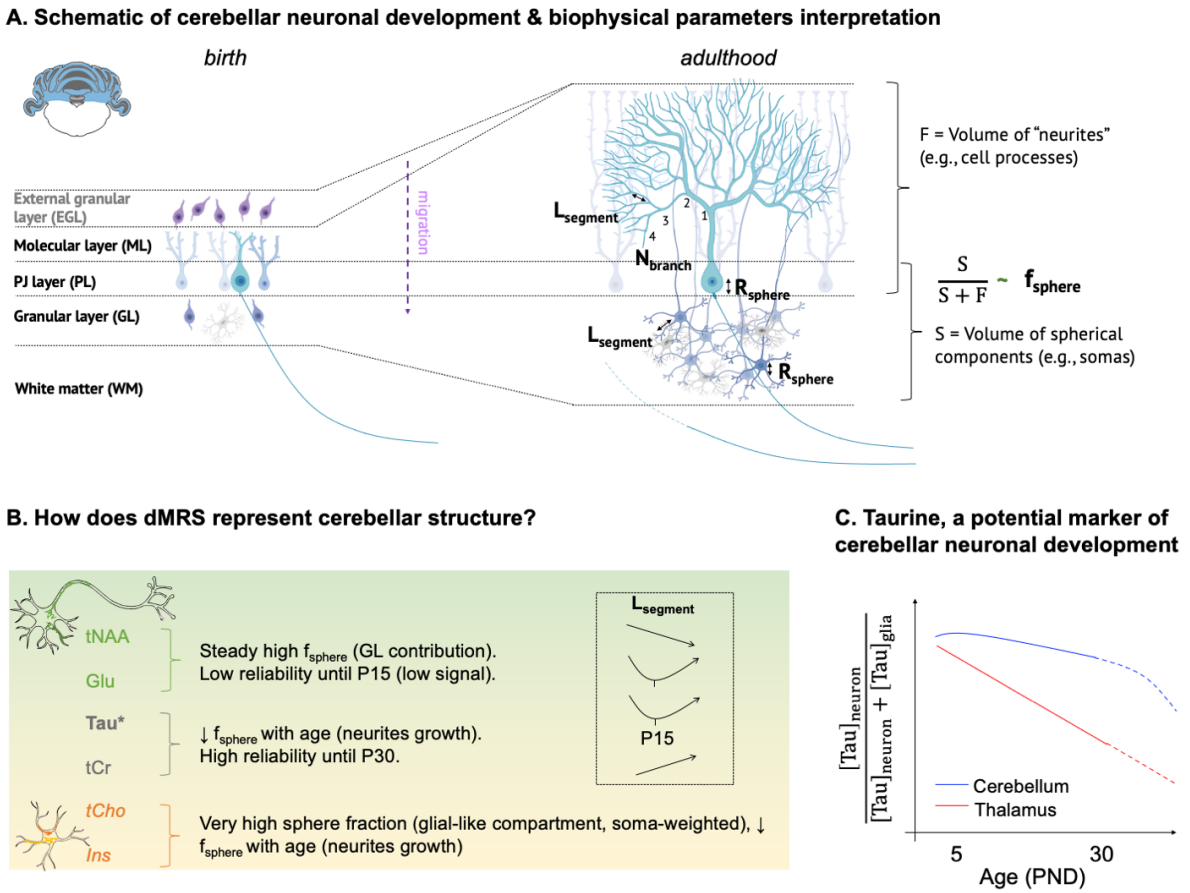

Figure 5: **The biophysical parameters are interpreted based on the cerebellar microstructural development and main results are summarised**. (A) Schematic of cerebellar neuronal development and biophysical modelling parameters interpretation. $L_{segment}$ is interpreted as the distance between two branches of the dendritic tree, N_{Branch} as the number of embranchments. The sphere radius R_{sphere} is interpreted as the average soma radius (i.e. granule and Purkinje cells). The sphere fraction f_{sphere} represents the volume of sphere-like cell components (e.g., somas) over the volume of fibrous cell components (e.g., cell processes or "neurite"). The sphere fraction is therefore inversely related to the dendritic tree growth. (B) Summary of the cerebellar results (C) Taurine seems to change compartment in the thalamus with age, going from neuronal-like compartments (low sphere fraction) to glial-like compartment (high sphere fraction), also indicated by its important signal drop with age. It suggests that taurine is a marker of neuronal maturation. Its concentration remains high up to P30 in the cerebellum. Taurine properties in the cerebellum (decreasing sphere fraction + relatively low sphere fractions) and contrast with the thalamus suggest that taurine could be a marker of cerebellar neuronal development.

While soma morphologic maturation mostly happens in the first week (McKay et al., 2005), the dendritic expansion bursts before P15 but continues to mature up to the end of the 4th week (McKay et al, 2005; Beekhof et al., 2021). Remarkably, the sphere fraction extracted from the diffusion properties of tCr and Tau decreases with age in the cerebellum only, potentially underlining the drastic Purkinje cell growth between birth and adulthood. Interestingly, the diffusion properties of glial metabolites Ins and tCho also display a trend to sphere fraction decrease with age: among cerebellar peculiarities, Bergmann glia develops long processes along Purkinje cells. Bergmann glia growth could also play a role in the sphere fraction decrease of Tau and tCr.

As shown in[35], we confirm in this study the high spectroscopic signal in neonates of both tCr and Tau. They are the two most reliably quantified metabolites up to P15 in both regions (continuing for Tau in the cerebellum up to P30) and the estimates of their diffusion properties are the least noisy. The important decrease of Tau levels in the thalamus, the extreme sphere radius decrease and sphere fraction increase with age extracted from Tau diffusion properties may indicate a change in Taurine compartmentation with age in the thalamus. Note that Taurine has a higher D_{intra}[32] compared to the other metabolites, potentially affecting the parameter estimation given for Taurine. As described in Methods, the fit for taurine was substantially improved for $D_{intra} > 0.6$ µm^2/ms. The results for D_{intra}=0.7 µm^2/ms are similar for all metabolites (**Figure S7**), but it brings Taurine sphere radius estimation to plausible values. However, the increase in sphere fraction with age stays clear: at P5, f_{sphere}(Tau) nears f_{sphere}(tNAA), while at P30 f_{sphere}(Tau) nears f_{sphere}(tCho). We can reasonably hypothesize that Taurine is relatively more concentrated in neurons at birth and loses its neuronal compartmentalisation with neuronal maturation, ending up concentrated in glial cells. Moreover, the volume take by glial cells in the brain is lower than the volume taken by neurons: the taurine signal decrease matches the suggested switch. Taurine is crucial in early development, and it has been shown in cats (unable to synthetise Taurine, intaking it from their diet), that a lack of taurine delays cortical and cerebellar maturation[37]. Older immunohistochemistry studies associated taurine with Purkinje cells specifically[38,39]. Taurine levels in the cerebellum are still high at P30, in agreement with its protracted development. Moreover, Taurine decreasing sphere fraction indicates that it stays relatively highly concentred in neurons until P30, following the neuronal cerebellar growth and complexification (**Figure 5A&C**). Given that the low tNAA and Glu signal up to P10 included, particularly in the cerebellum, prevents a reliable exploitation of their diffusion properties, we suggest taurine as a cerebellar marker of early neuronal development, possibly more specifically to Purkinje cells. Total creatine stands as good marker too. However there is no indication of a preferential neuronal compartmentation for this metabolite during early development, hence it is less specific to neurons. This is comforted by the higher f_{sphere}(tCr) compared to f_{sphere}(Tau) up to P15 in the cerebellum.

We chose to interpret the dMRS data with an analytical spheres & "astrosticks" model and with a computational morphometric model. The analytical model was applied simultaneously to the signal attenuation at high b-values and the ADCs at long diffusion times, and on individual animals. In addition to the valuable biophysical biomarkers, it provides a good signal representation to evaluate the significance of the differences between diffusion properties of individual datasets. The experimental design was not suitable for a randomly oriented infinite cylinders ("astrocylinders") model as in previous studies (Palombo et al., 2017; Ligneul et al., 2019). The mixing time used for the acquisition of signal decay at high b-values (TM=100 ms) is too long to enable sensitivity to fibre radius (Ligneul, Najac et al., 2023), hence the choice of "astrosticks" model. The sphere compartment was added to account for the high sphere fraction in the cerebellum, and for the nature of the neonatal brain (under-developed neurons). The RMSEs from the different models tested (**Figure S2**) tend to be more similar at P30: the sphere compartment loses its importance for modelling the adult brain.

The computational morphometric model was applied to attempt to extract cell extension related parameters, but the study design and data quality are suboptimal, and we could only reliably extract

$L_{segment}$ and D_{intra} (**Figure S6**). D_{intra} is mostly stable with age in both regions. However, it sometimes drops or peaks, likely affecting the other parameters' estimations. The longest mixing time (TM=1000 ms) is short compared to previous studies using a similar modelling approach (Palombo et al., 2016; Ligneul et al., 2019), meaning that the diffusion path is shorter (i.e., about 30µm in this study compared to about 45µm in previous studies, assuming D_{intra}=0.5 µm^2/ms). Note that the higher D_{intra} of Tau is therefore an asset for probing early neuronal cerebellar growth. In our study, the number of embranchments (N_{branch}) was very poorly evaluated because of the high level of noise in the data. However, even with a better dataset quality and a more optimal study design, it is unlikely that the N_{branch} estimation could reflect the Purkinje cell morphometry because of their size and complexity in adulthood.

Although tNAA is poorly evaluated before P15, it is surprising that the estimated $L_{segment}$ consistently decreases in the cerebellum with age. $L_{segment}$ also increase for tCr, Tau and Glu diffusion properties from P15, but it seems that there it decreases first up to P15 and then increase again for Tau and Glu, forming a U-shape curve. This could reflect the complexification of the dendritic tree following its expansion. Beekhof and colleagues[3] indicate that the molecular layer grows rapidly, but that the Purkinje cells continue to complexify up to the 4th week. To better understand these results, we extracted the morphometries of developing Purkinje cells and developing thalamic interneurons (both in the mouse) from 3DNeuroMorph.org. Interestingly, it shows a decrease in $L_{segment}$ up to P13 for Purkinje cells, whilst being quite stable in the thalamus (**Figure 6**).

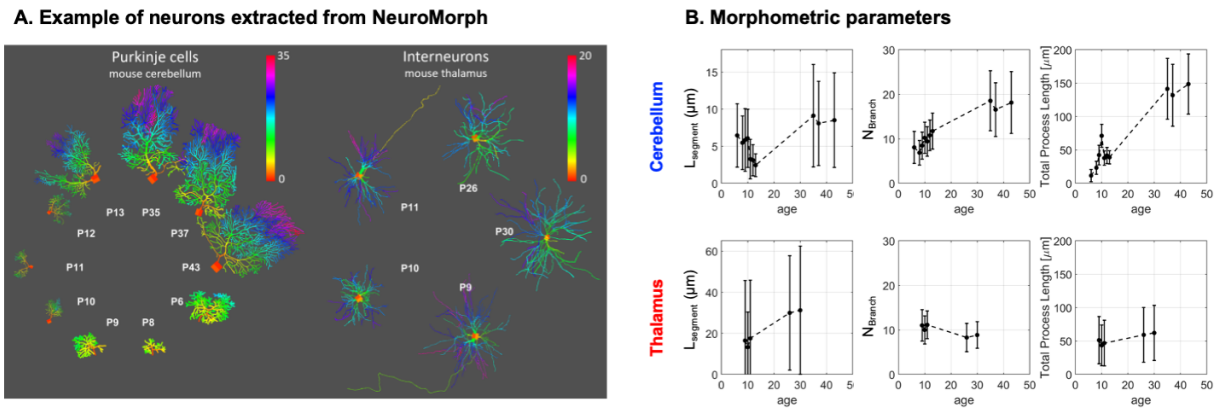

Figure 6: Morphometric parameters extracted from mouse real cells 3D reconstructions on NeuroMorph shows a decrease of $L_{segment}$ up to P13 in developing cerebellar Purkinje cells, but not in developing thalamic interneurons. (A) Examples of cells extracted from NeuroMorph. Total number of cells used per age and region are given in Supplementary Material. References: Cerebellum P6-P10[40], P10-P13[41], P35-P43[42]; Thalamus P9-P30[43] (B) The values of Branch Length (Lsegment), Branching Order and total process length are directly estimated from the morphology using the function stat_tree in the Trees Matlab Toolbox.

Conclusion

This study successfully used diffusion-weighted MRS to longitudinally and non-invasively measure cell-specific cerebellar and thalamic microstructural features during early development in rat neonates. Notably, we show the sensitivity of Taurine to early neuronal cerebellar development. This is a stepping-stone enabling further studies in pathological conditions.

Funding

This work was funded by Wellcome. *The Wellcome Centre for Integrative Neuroimaging is supported by core funding from the Wellcome Trust (203139/Z/16/Z and 203139/A/16/Z).* MP is supported by UKRI Future Leaders Fellowship (MR/T020296/1)

REFERENCES

1. Szulc KU, Lerch JP, Nieman BJ, et al. 4D MEMRI atlas of neonatal FVB/N mouse brain development. *Neuroimage*. 2015;118:49-62. doi:10.1016/j.neuroimage.2015.05.029

2. Sathyanesan A. Emerging connections between cerebellar development , behaviour and complex brain disorders. *Nat Rev Neurosci*. 2019;20(May). doi:10.1038/s41583-019-0152-2

3. Beekhof GC, Osorio C, White JJ, et al. Differential spatiotemporal development of Purkinje cell populations and cerebellum-dependent sensorimotor behaviors. *Elife*. 2021:1-34.

4. Fatemi SH, Halt AR, Realmuto G, et al. Purkinje Cell Size is Reduced in Cerebellum of Patients With Autism. *Cell Mol Neurobiol*. 2002;22(2):171-175.

5. Tsai PT, Hull C, Chu Y, et al. Autistic-like behaviour and cerebellar dysfunction in Purkinje cell Tsc1 mutant mice. *Nature*. 2012;488(7413):647-651. doi:10.1038/nature11310

6. Cupolillo D, Hoxha E, Faralli A, et al. Autistic-Like Traits and Cerebellar Dysfunction in Purkinje Cell PTEN Knock-Out Mice. *Neuropsychopharmacology*. 2016;41:1457-1466. doi:10.1038/npp.2015.339

7. Yamashiro K, Hori K, Lai ESK, et al. AUTS2 Governs Cerebellar Development, Purkinje Cell Maturation, Motor Function and Social Communication. *iScience*. 2020;23(12):101820. doi:10.1016/j.isci.2020.101820

8. Kim J, Kwon N, Chang S, et al. Altered branching patterns of Purkinje cells in mouse model for cortical development disorder. *Sci Rep*. 2011:1-7. doi:10.1038/srep00122

9. Robinson L, Guy J, Mckay L, et al. Morphological and functional reversal of phenotypes in a mouse model of Rett syndrome. *Brain*. 2012;135(January). doi:10.1093/brain/aws096

10. Usui N, Co M, Harper M, Rieger MA, Dougherty JD, Konopka G. Sumoylation of FOXP2 Regulates Motor Function and Vocal Communication Through Purkinje Cell Development. *Biol Psychiatry*. 2017;81(3):220-230. doi:10.1016/j.biopsych.2016.02.008

11. Sundberg M, Tochitsky I, Buchholz DE, et al. Purkinje cells derived from TSC patients display hypoexcitability and synaptic de fi cits associated with reduced FMRP levels and reversed by rapamycin. *Mol Psychiatry*. 2018;23:2167-2183. doi:10.1038/s41380-018-0018-4

12. Hwang WJ, Kwak Y Bin, Cho KIK, et al. Thalamic Connectivity System Across Psychiatric Disorders : Current Status and Clinical Implications. *Biol Psychiatry Glob Open Sci*. 2022;2(4):332-340. doi:10.1016/j.bpsgos.2021.09.008

13. Krol A, Wimmer RD, Halassa MM, Feng G. Thalamic Reticular Dysfunction as a Circuit Endophenotype in Neurodevelopmental Disorders. *Neuron*. 2018;98(2):282-295. doi:10.1016/j.neuron.2018.03.021

14. Antón-Bolaños N, Espinosa A, Lopew-Bendito G. Developmental interactions between thalamus and cortex : a true love reciprocal story. *Curr Opin Neurobiol*. 2018;52:33-41. doi:10.1016/j.conb.2018.04.018

15. Sato H, Hatakeyama J, Iwasato T, Araki K. Thalamocortical axons control the cytoarchitecture of neocortical layers by specific supply of VGF. *Elife*. 2022:1-23.

16. Alexander DC, Dyrby TB, Nilsson M. Imaging brain microstructure with diffusion MRI : practicality and applications. *NMR Biomed*. 2019;32(September 2017):1-26. doi:10.1002/nbm.3841

17. Ronen I, Valette J. Diffusion-Weighted Magnetic Resonance Spectroscopy. *eMagRes*. 2015;4(1):733-750. doi:10.1002/9780470034590.emrstm1471

18. Palombo M, Ligneul C, Najac C, et al. New paradigm to assess brain cell morphology by diffusion-weighted MR spectroscopy in vivo. *Proc Natl Acad Sci U S A*. 2016;113(24):6671-6676. doi:10.1073/pnas.1504327113

19. Palombo M, Ligneul C, Valette J. Modeling Diffusion of Intracellular Metabolites in the Mouse Brain up to Very High Diffusion-Weighting : Diffusion in Long Fibers (Almost) Accounts for Non-Monoexponential Attenuation. *Magn Reson Med*. 2017;350(November 2016):343-350. doi:10.1002/mrm.26548

20. Ligneul C, Palombo M, Hernández-Garzón E, et al. Diffusion-weighted magnetic resonance spectroscopy enables cell-specific monitoring of astrocyte reactivity in vivo. *Neuroimage*. 2019;191(December 2018):457-469. doi:10.1016/j.neuroimage.2019.02.046

21. Genovese G, Millecamps A, Abdoulkader N, et al. Inflammation-driven glial alterations in the cuprizone mouse model probed with diffusion-weighted magnetic resonance spectroscopy at 11 . 7 T. *NMR Biomed*. 2021;(January):1-13. doi:10.1002/nbm.4480

22. Ercan E, Magro-checa C, Valabregue R, et al. Glial and axonal changes in systemic lupus erythematosus measured with diffusion of intracellular metabolites. *Brain*. 2016;139:1447-1457. doi:10.1093/brain/aww031

23. De Marco R, Ronen I, Branzoli F, et al. Diffusion-weighted MR spectroscopy (DW-MRS) is sensitive to LPS-induced changes in human glial morphometry : A preliminary study. *Brain Behav Immun*. 2022;99(October 2021):256-265.

24. Qiu LR, Fernandes DJ, Szulc-Lerch KU, et al. Mouse MRI shows brain areas relatively larger in males emerge before those larger in females. *Nat Commun*. 2018;9(1). doi:10.1038/s41467-018-04921-2

25. Fatemi SH, Folsom TD. The Neurodevelopmental Hypothesis of Schizophrenia, Revisited. *Schizophr Bull*. 2009;35(3):528-548. doi:10.1093/schbul/sbn187

26. Ismail FY, Shapiro BK. What are neurodevelopmental disorders ? *Curr Opin Neurol*. 2019:611-616. doi:10.1097/WCO.0000000000000710

27. Takeuchi Y, Asano H, Katayama Y, Muragaki Y, Imoto K, Miyata M. Large-Scale Somatotopic Refinement via Functional Synapse Elimination in the Sensory Thalamus of Developing Mice. *J Neurosci*. 2014;34(4):1258-1270. doi:10.1523/JNEUROSCI.3865-13.2014

28. Ligneul C, Andersson J, Jbabdi S, Lerch J, Clarke WT. Rejecting or retaining motion corrupted transients in di ff usion- weighted MRS : high b-values and multiple directions. In: *Proc. Intl. Soc. Mag. Reson. Med. 31 (2023)*. Vol 31. ; 2023:3934.

29. Coupé P, Yger P, Prima S, Hellier P, Kervrann C, Barillot C. An Optimized Blockwise Nonlocal Means Denoising Filter for 3-D Magnetic Resonance Images. *IEEE Trans Med Imaging*. 2008;27(4):425-441.

30. Goerzen D, Fowler C, Devenyi GA, et al. An MRI-Derived Neuroanatomical Atlas of the Fischer 344 Rat Brain. *Sci Rep*. 2020;10:1-13. doi:10.1038/s41598-020-63965-x

31. Friedel M, Eede MC Van, Pipitone J, Chakravarty MM, Lerch JP. Pydpiper : a flexible toolkit for constructing novel registration pipelines. *Front Neuroinform*. 2014;8(July):1-21. doi:10.3389/fninf.2014.00067

32. Ligneul C, Valette J. Probing metabolite diffusion at ultra-short time scales in the mouse brain

using optimized oscillating gradients and “short”-echo-time diffusion-weighted MRS. *NMR Biomed*. 2017;30(1):1-10. doi:10.1002/nbm.3671

33. Marchadour C, Brouillet E, Hantraye P, Lebon V, Valette J. Anomalous diffusion of brain metabolites evidenced by diffusion-weighted magnetic resonance spectroscopy in vivo. *J Cereb Blood Flow Metab*. 2012;32(August). doi:10.1038/jcbfm.2012.119

34. Kuznetsova A. lmerTest Package : Tests in Linear Mixed Effects Models. *J Statis*. 2017;82(13). doi:10.18637/jss.v082.i13

35. Tkac I, Rao R, Georgieff MK, Gruetter R. Developmental and Regional Changes in the Neurochemical Profile of the Rat Brain Determined by In Vivo 1 H NMR Spectroscopy. *Magn Reson Med*. 2003;32:24-32. doi:10.1002/mrm.10497

36. Ligneul C, Palombo M, Valette J. Metabolite diffusion up to very high b in the mouse brain in vivo: Revisiting the potential correlation between relaxation and diffusion properties. *Magn Reson Med*. 2017;77(4):1390-1398. doi:10.1002/mrm.26217

37. Aerts L, Van Assche FA. Taurine and taurine-deficiency in the perinatal period. *J Perinat Med*. 2002;30:281-286.

38. Madsen S, Ottersen OLEP, Storm-mathisen JON. IMMUNOCYTOCHEMICAL VISUALIZATION OF TAURINE: NEURONAL LOCALIZATION IN THE RAT CEREBELLUM. *Neurosci Lett*. 1985;60:255-260.

39. Magnusson KR, Madl JE, Clements JR, Wu J-Y, Larson AA, Beitz AJ. Colocalization of Taurine- and Cysteine Sulfinic Acid Decarboxylase- like lmmunoreactivity in the Cerebellum of the Rat with Monoclonal Antibodies Against Taurine. *J Neurosci*. 1988;8(December).

40. Fukumitsu K, Hatsukano T, Yoshimura A, Heuser J. Mitochondrial fission protein Drp1 regulates mitochondrial transport and dendritic arborization in cerebellar Purkinje cells. *Mol Cell Neurosci*. 2016;71:56-65. doi:10.1016/j.mcn.2015.12.006

41. Jayabal S, Ljungberg L, Watt AJ. Transient cerebellar alterations during development prior to obvious motor phenotype in a mouse model of spinocerebellar ataxia type 6. *J Physiol*. 2017;3:949-966. doi:10.1113/JP273184

42. Chen XR, Heck N, Lohof AM, et al. Mature Purkinje Cells Require the Retinoic Acid-Related Orphan Receptor- alpha-ROR alpha to Maintain Climbing Fiber Mono-Innervation and Other Adult Characteristics. *J Neurosci*. 2013;33(22):9546-9562. doi:10.1523/JNEUROSCI.2977-12.2013

43. Hetsch F, Wang D, Chen X, et al. CKAMP44 controls synaptic function and strength of relay neurons during early development of the dorsal lateral geniculate nucleus. *J Physiol*. 2022;15:3549-3565. doi:10.1113/JP283172